Chem, Volume *8*

Supplemental information

Highly effective conversion of CO_2 into light olefins abundant in ethene

Sen Wang, Li Zhang, Pengfei Wang, Xingchen Liu, Yanyan Chen, Zhangfeng Qin, Mei Dong, Jianguo Wang, Lin He, Unni Olsbye, and Weibin Fan

Supplemental Information

Supplemental data items

Table S1. Physicochemical properties of various Cr_2O_3 oxides. [a]

Catalysts	Phase	S_{BET} (m^2 g^{-1})	V_{mirco} (cm^3 g^{-1})	d_{size} (nm)	D_{size} (nm)	Cell parameter			
						a (Å)	b (Å)	c (Å)	volume ($Å^3$)
Cr_2O_3(SG)	Hexagonal	60.8	0.35	16.1	24.2	4.959	4.959	13.598	289.69
Cr_2O_3(CP)	Hexagonal	35.6	0.08	8.3	28.6	4.946	4.946	13.571	287.52

[a] Cr_2O_3(SG) and Cr_2O_3(CP) represent the Cr_2O_3 oxides prepared by the sol-gel and co-precipitation methods respectively. The phase structures and cell parameter of these two Cr_2O_3 oxides were identified and calculated by the Rietveld refinement of their XRD patterns. The surface area (S_{BET}), pore volume (V_{mirco}) and average pore size (d_{size}) were obtained from their N_2 physisorption isotherms by the BET, t-plot and BJH methods, respectively. The mean particle sizes (D_{size}) were estimated by the Scherrer equation.

Figure S1.

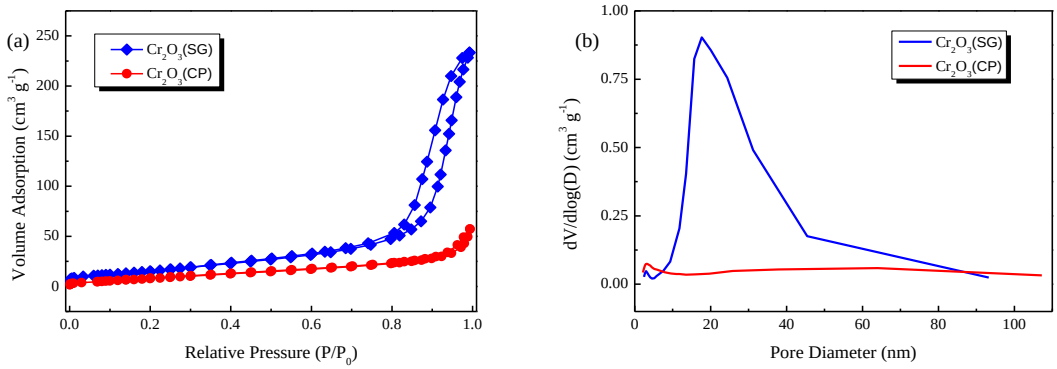

Figure S1. N_2 sorption isotherms (a) and corresponding pore size distributions (b) of Cr_2O_3(SG) and Cr_2O_3(CP).

Figure S2.

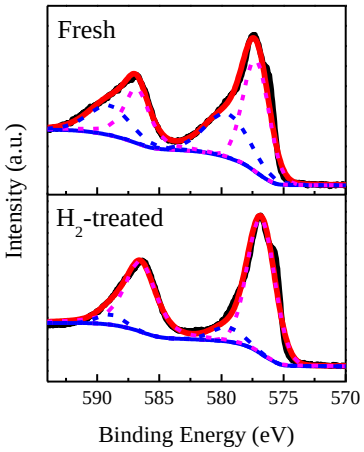

Figure S2. In situ Cr(2p) XPS of fresh and H_2-treated Cr_2O_3(SG).

50 mg Sample was placed in the in situ cell and pretreated at 400 ºC for 2 h in a H_2 flow (30 mL/min). Then, it was purged with Ar (20 mL/min) for 0.5 h. Afterwards, the in situ cell was transferred from the auxiliary pretreatment chamber to the XPS measurement chamber under high vacuum conditions.

Table S2. Crystalline phase structures and cell parameters of fresh and H_2-treated (400 ºC for 2 h) Cr_2O_3(SG). [a]

Catalysts	Phase	D_{size} (nm)	Cell parameter			
			a (Å)	b (Å)	c (Å)	volume (Å^3)
Cr_2O_3 (fresh)	Hexagonal	24.2	4.959	4.959	13.598	289.69
Cr_2O_3 (H_2-treated)	Hexagonal	26.8	4.977	4.977	13.619	292.26

[a] The crystalline phase structures and cell parameters of fresh and H_2-treated Cr_2O_3(SG) were determined by the Rietveld refinement of XRD patterns. The mean particle sizes (D_{size}) of fresh and H_2-treated Cr_2O_3(SG) were estimated by the Scherrer equation.

Figure S3.

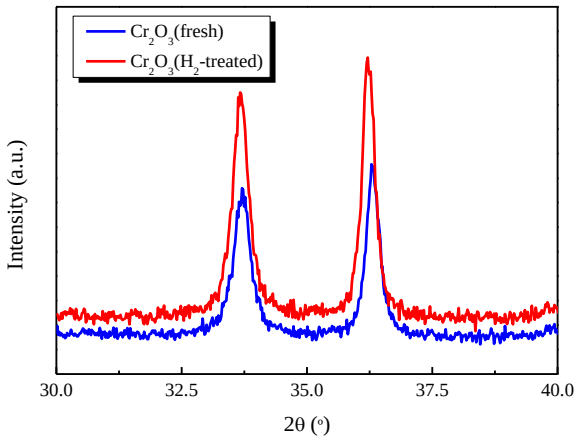

Figure S3. In situ XRD patterns of fresh and H_2-treated (400 ºC for 2 h) Cr_2O_3(SG) in the 2θ region from 30.0º to 40.0°.

Figure S4.

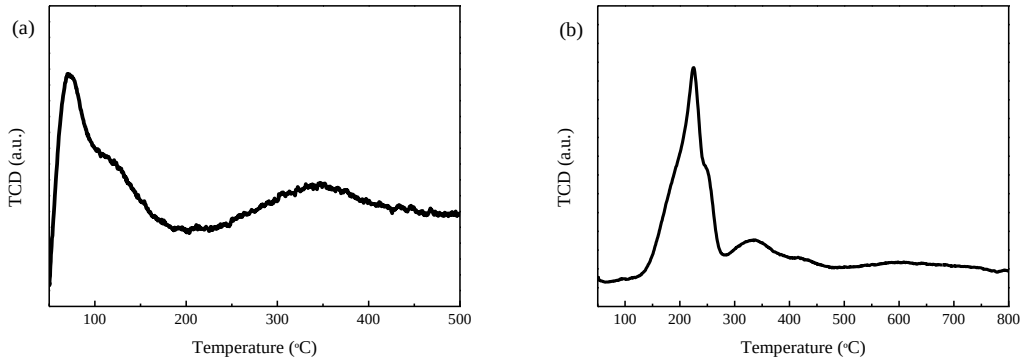

Figure S4. CO_2-TPD (a) and H_2-TPR (b) profiles of Cr_2O_3(SG).

Figure S5.

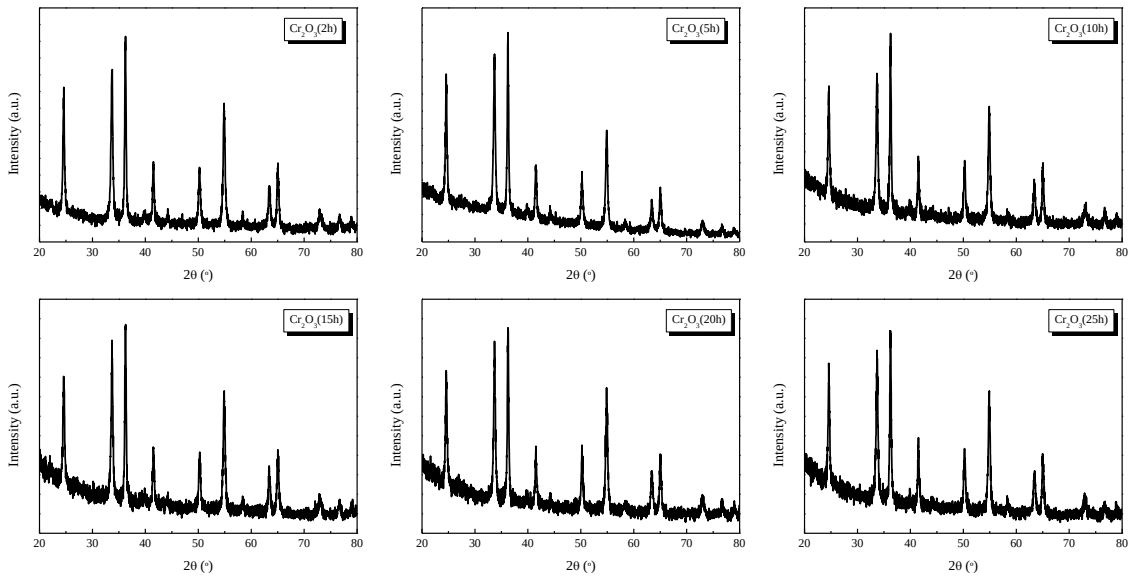

Figure S5. In situ XRD patterns of Cr_2O_3(SG) for hydrogenation of CO_2 at 370 ºC for different reaction time. The sample powder was first placed in a self-made cell and pretreated at 400 ºC for 2 h in a H_2 flow (30 mL/min). Then, it was purged with an Ar flow (30 mL/min) for 0.5 h. After the sample was cooled to the reaction temperature (370 ºC), a CO_2/H_2 gaseous mixture (composed of H_2 flow (30 mL/min) and CO_2 flow (10 mL/min)) was continuously introduced in the cell. The XRD patterns were collected after the reaction was carried out for 2, 5, 10, 15, 20 and 25 h, respectively.

Table S3. Crystalline phase structures and cell parameter of Cr_2O_3(SG) after catalyzing the CO_2 hydrogenation for different time. [a]

Catalysts	Phase	D_{size} (nm)	Cell parameter			
			a (Å)	b (Å)	c (Å)	volume (Å^3)
Cr_2O_3-2 h	Hexagonal	25.4	4.976	4.976	13.617	292.04
Cr_2O_3-5 h	Hexagonal	24.9	4.976	4.976	13.615	291.92
Cr_2O_3-10 h	Hexagonal	26.4	4.976	4.976	13.618	292.06
Cr_2O_3-15 h	Hexagonal	25.7	4.977	4.977	13.620	292.27
Cr_2O_3-20 h	Hexagonal	25.1	4.977	4.977	13.619	292.14
Cr_2O_3-25 h	Hexagonal	25.1	4.978	4.978	13.619	292.32

[a] The phase structures and cell parameters of Cr_2O_3(SG) after catalyzing the CO_2 hydrogenation at 370 ºC for different reaction time were identified and calculated by the Rietveld refinement of in situ XRD patterns. The mean particle sizes were estimated by the Scherrer equation.

Figure S6.

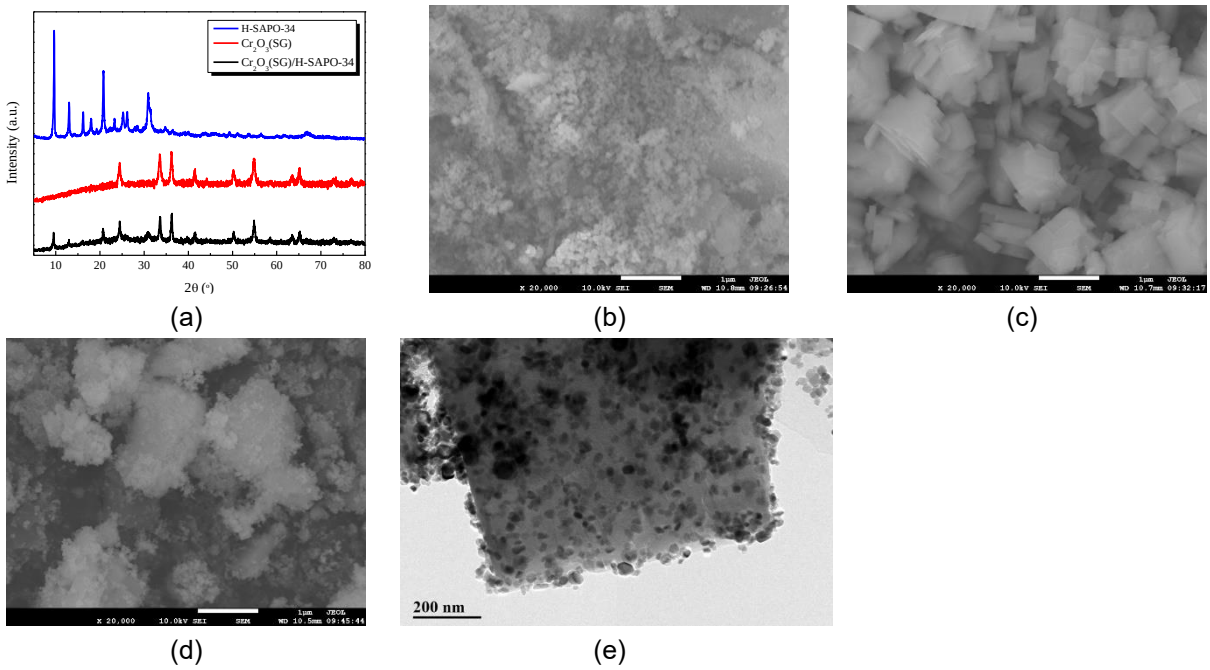

Figure S6. XRD patterns (a) of Cr_2O_3(SG), H-SAPO-34, and Cr_2O_3(SG)/H-SAPO-34 composite, SEM images of Cr_2O_3(SG) (b), H-SAPO-34 (c), and Cr_2O_3(SG)/H-SAPO-34 composite (d), and TEM image (e) of Cr_2O_3(SG)/H-SAPO-34 composite.

Table S4. Physicochemical properties of Cr_2O_3(SG), H-SAPO-34 and Cr_2O_3(SG)/H-SAPO-34 composite. [a]

Catalysts	Phase	S_{BET} ($m^2\ g^{-1}$)	V_{mirco} ($cm^3\ g^{-1}$)	d_{size} (nm)
Cr_2O_3(SG)	Hexagonal	60.8	0.35	16.1
H-SAPO-34	Cubic	466.9	0.44	9.2
Cr_2O_3(SG)/H-SAPO-34	Hexagonal+cubic	262.1	0.24	7.6

[a] The surface area (S_{BET}), pore volume (V_{mirco}) and average pore size (d_{size}) were obtained from the N_2 sorption isotherm by the BET, t-plot and BJH methods, respectively.

Figure S7.

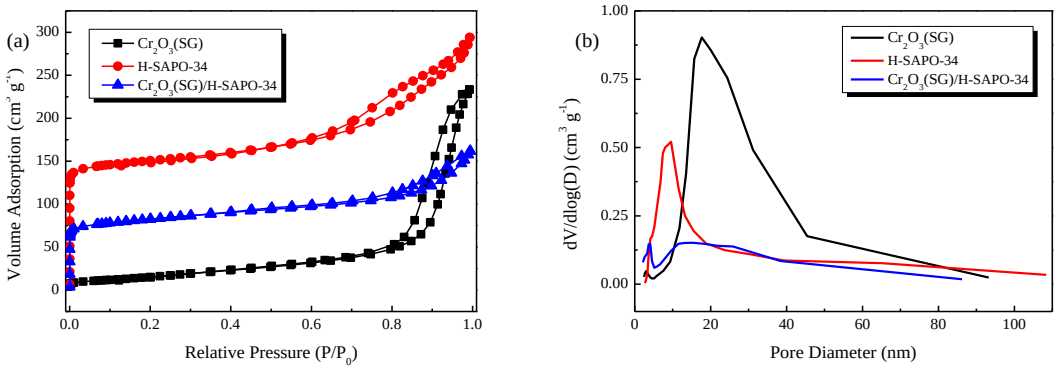

Figure S7. N_2 sorption isotherms (a) and corresponding pore size distributions (b) of Cr_2O_3(SG), H-SAPO-34 and Cr_2O_3(SG)/H-SAPO-34 composite catalyst.

Figure S8.

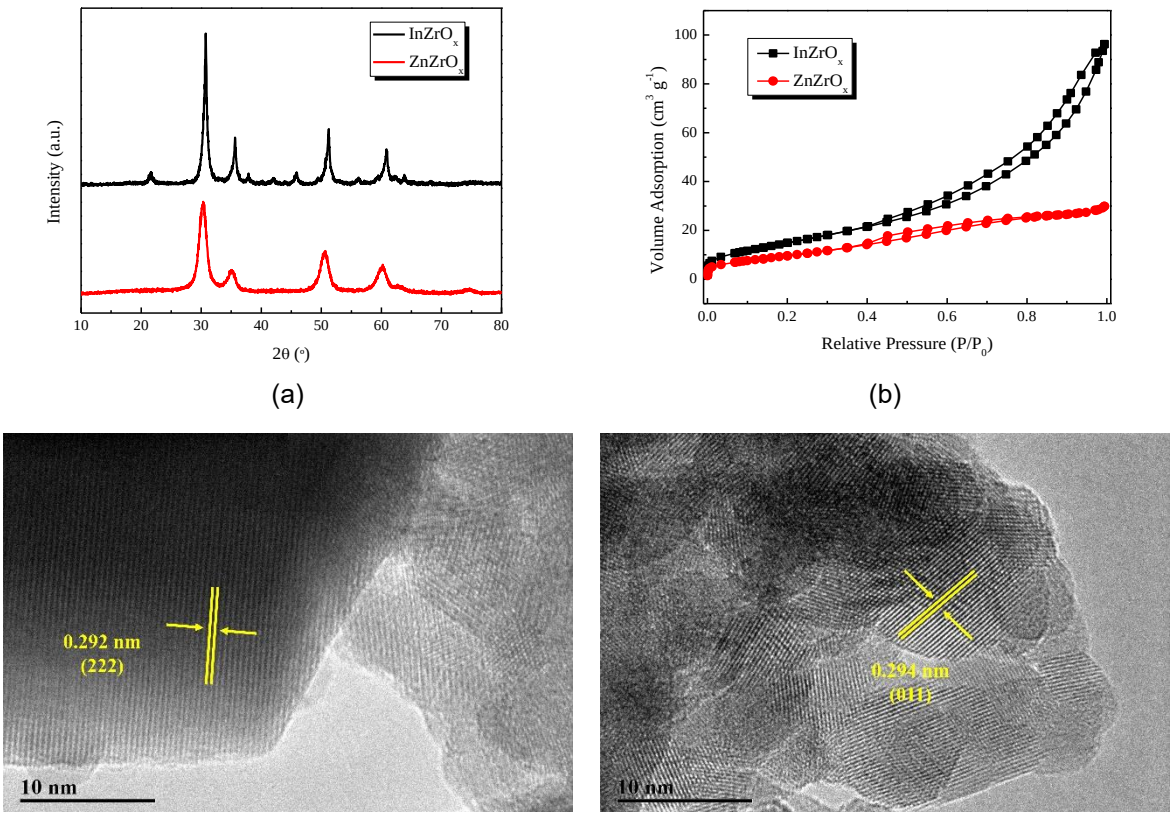

Figure S8. XRD patterns (a), N_2 sorption isotherms (b) and HRTEM images of $InZrO_x$ (c) and $ZnZrO_x$ (d).

Figure S9.

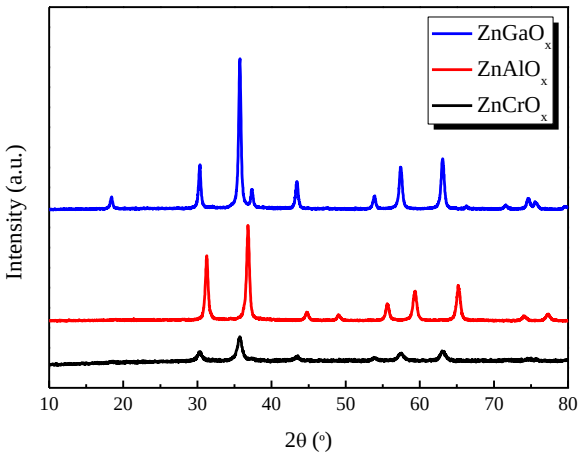

Figure S9. XRD patterns of $ZnCrO_x$, $ZnAlO_x$ and $ZnGaO_x$.

Table S5. Physicochemical properties of $InZrO_x$ and $ZnZrO_x$ oxides. [a]

Catalysts	Phase	S_{BET} (m^2 g^{-1})	V_{mirco} (cm^3 g^{-1})	d_{size} (nm)	D_{size} (nm)	Cell parameter			
						a (Å)	b (Å)	c (Å)	volume ($Å^3$)
$InZrO_x$	Cubic	58.0	0.14	8.4	14.8	10.112	10.112	10.112	1034.12
$ZnZrO_x$	Tetragonal	37.6	0.05	4.4	5.6	3.591	3.591	5.154	66.46

[a] The phase structures and cell parameter of $InZrO_x$ and $ZnZrO_x$ oxides were determined by the Rietveld refinement of their XRD patterns. The surface area (S_{BET}), pore volume (V_{mirco}) and average pore size (d_{size}) were obtained from nitrogen physisorption isotherm by the BET, t-plot and BJH methods, respectively. The mean particle sizes (D_{size}) were calculated by the Scherrer equation.

Figure S10.

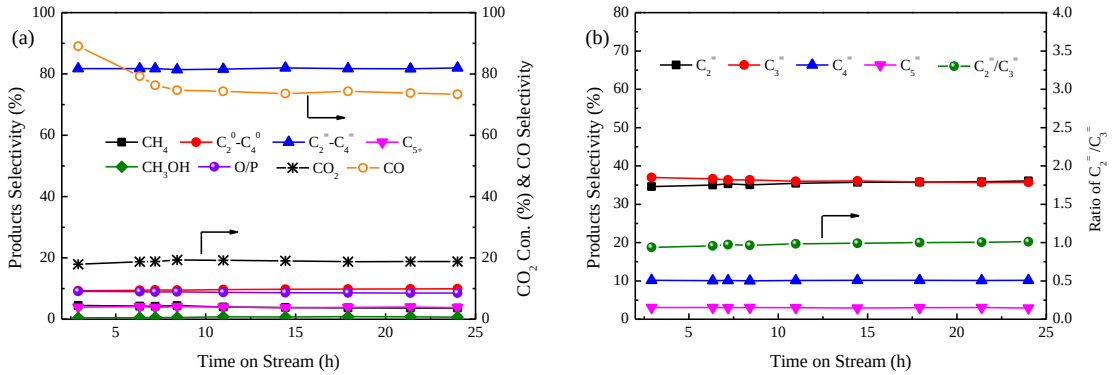

Figure S10. CO_2 conversion and product distribution for hydrogenation of CO_2 to light olefins on $ZnCrO_x$/H-SAPO-34 (typical reaction conditions: H_2/CO_2 = 3:1, GHSV = 4000 mL/(g·h), 0.5 MPa and 370 °C).

Table S6. Catalytic results of various metal oxide/H-SAPO-34 composite catalysts for direct conversion of CO_2 into light olefins.

	Temperature & pressure	CO_2 con. (%)	CO sel. (%)	CH_4 (%)	$C_2^=$–$C_4^=$ (%)	$C_2^=$ (%)	$C_2^=$ yield (%)	$C_2^=/C_3^=$ ratio	
Cr_2O_3(SG)/H-SAPO-34 [a]	370 °C, 0.5 MPa	13.1	36.0	1.2	95.7	71.0	6.0	3.1	This work
In_2O_3-ZrO_2 /H-SAPO-34	400 °C, 3.0 MPa	35.5	80.0	5.0	76.4	--	--	--	Ref.1
In-Zr/H-SAPO-34	380 °C, 3.0 MPa	26.2	63.9	2.0	74.5	--	--	--	Ref.2
In-Zr/H-SAPO-34	400 °C, 1.5 MPa	15.0	85.0	3.0	85.0	35.0	0.8	0.70	Ref.3
In_2O_3/H-SAPO-34	380 °C, 2.5 MPa	35.0	80.0	3.0	68.0	20.0	1.4	0.50	Ref.4
ZnZrO/H-SAPO-34	380 °C, 2.0 MPa	12.6	47.0	3.0	80.0	28.0	1.9	0.65	Ref.5
$ZnGa_2O_4$/H-SAPO-34	370 °C, 3.0 MPa	13.0	50.0	1.0	86.0	--	--	--	Ref.6
$ZnAl_2O_4$/H-SAPO-34	370 °C, 3.0 MPa	15.0	49.0	0.7	87.0	--	--	--	Ref.7
In_2O_3-ZrO_2/SAPO-5	300 °C, 3.0 MPa	6.7	56.0	3.0	83.0 [b]	14.0 [b]	0.5 [b]	0.93 [b]	Ref.8
CuOZnOZrO_2 /H-SAPO-34	400 °C, 2.0 MPa	19.6	58.6	14.6	60.5	24.2	1.9	0.60	Ref.9

[a] The data were obtained from Figure 2(e) and Figure 2(f) in the main text.

[b] The selectivity to corresponding alkene and alkane.

Figure S11.

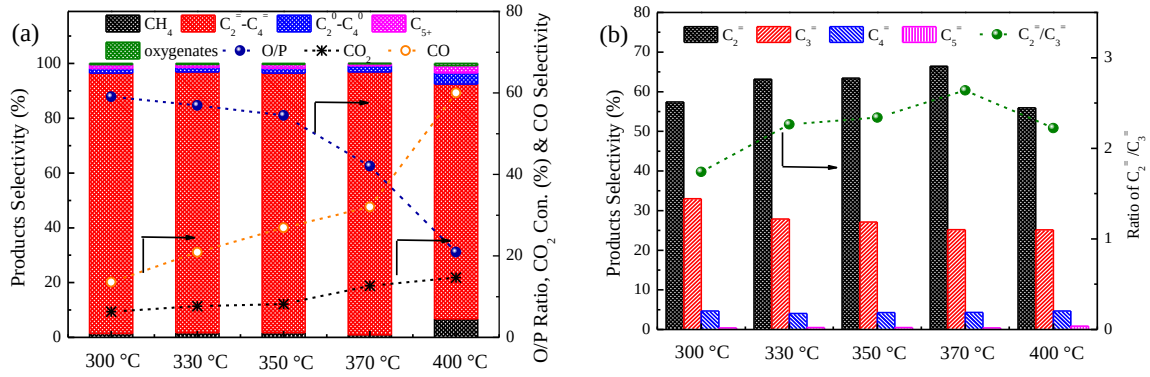

Figure S11. Effect of reaction temperature on the catalytic performance of Cr_2O_3(SG)/H-SAPO-34 composite for direct hydrogenation of CO_2 into light olefins (reaction conditions: H_2/CO_2 = 3/1, 0.5 MPa and GHSV = 4000 mL/(g·h)).

Figure S12.

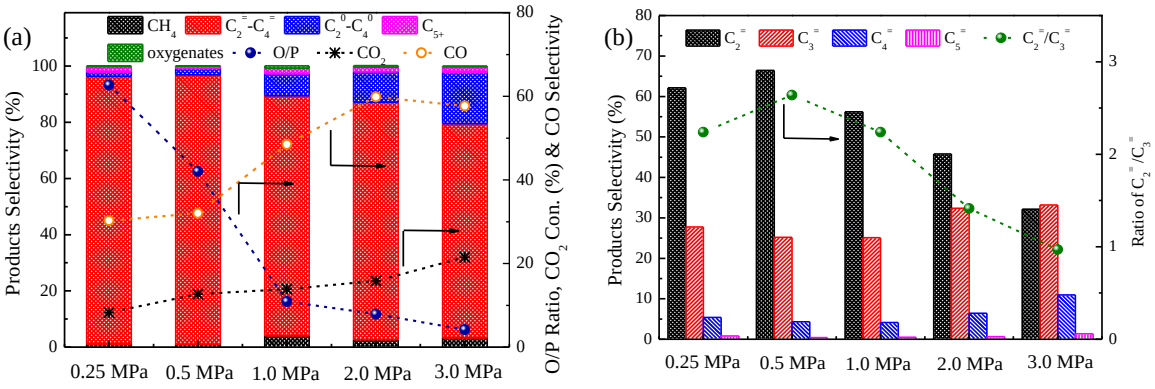

Figure S12. Effect of reaction pressure on the catalytic performance of Cr_2O_3(SG)/H-SAPO-34 composite catalyst for direct hydrogenation of CO_2 into light olefins (reaction conditions: H_2/CO_2 = 3/1, 370 °C and GHSV = 4000 mL/(g·h)).

Figure S13.

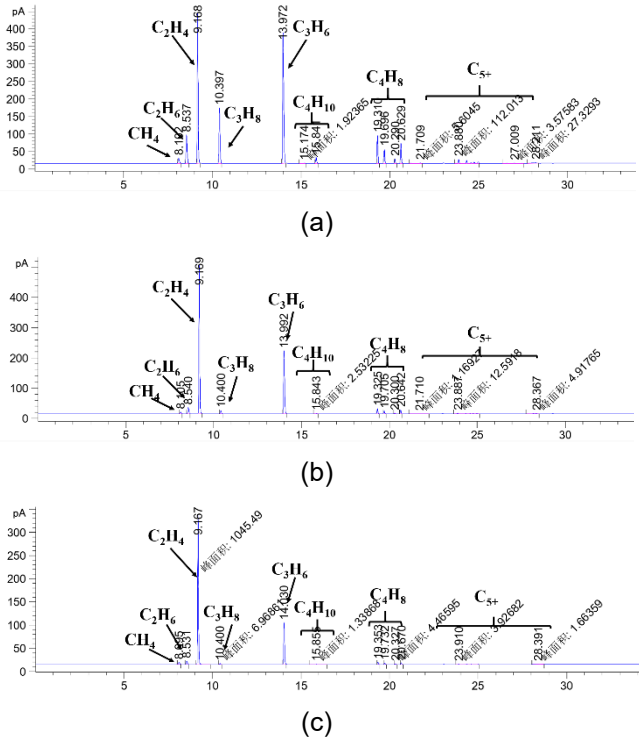

Figure S13. GC chromatograms for conversion of CO_2 into light olefins on Cr_2O_3(SG)/H-SAPO-34 composite catalyst at 370 °C and 3.0 MPa (a), 1.0 MPa (b) and 0.5 MPa (c).

Figure S14.

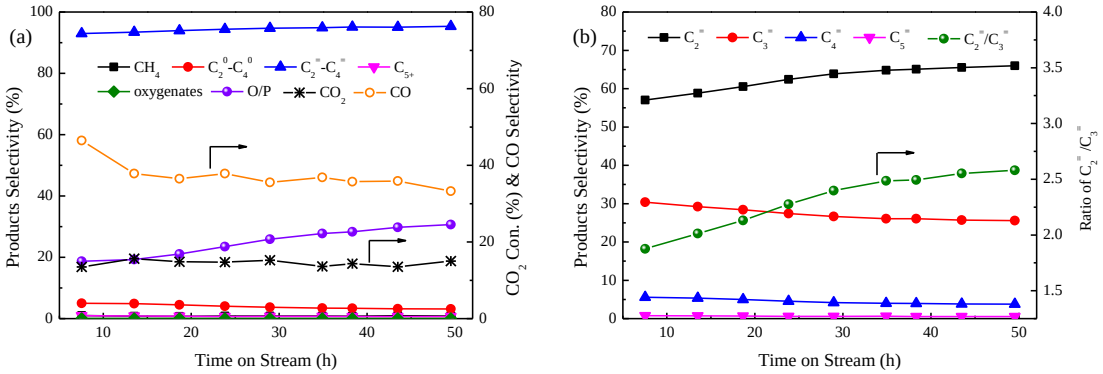

Figure S14. Dependences of CO_2 conversion and product distribution on the reaction time obtained on Cr_2O_3(SG)/H-SAPO-34 (typical reaction conditions: 0.5 MPa, 370 °C, H_2/CO_2 = 6:1 and GHSV = 4000 mL/(g·h)).

Figure S15.

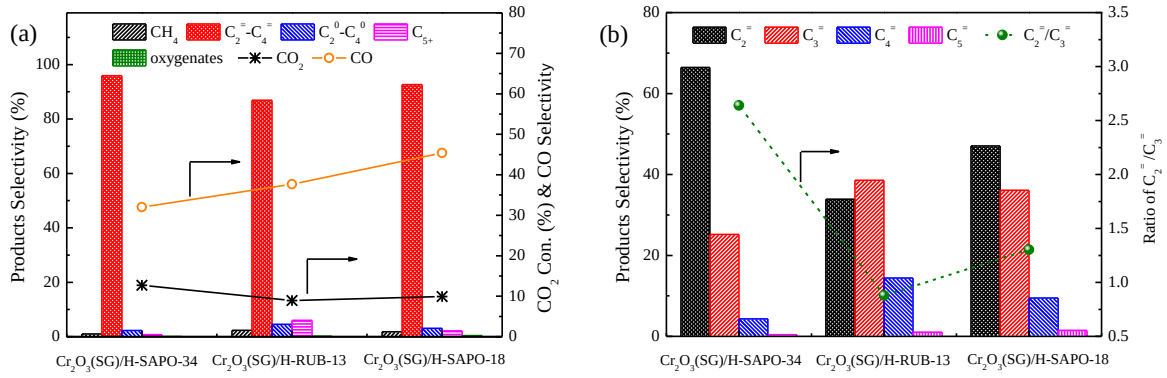

Figure S15. CO_2 conversion and product distribution obtained over Cr_2O_3(SG) and various zeolites composite catalysts (reaction conditions: H_2/CO_2 = 3:1, GHSV = 4000 mL/(g·h), 0.5 MPa, 370 °C).

Figure S16.

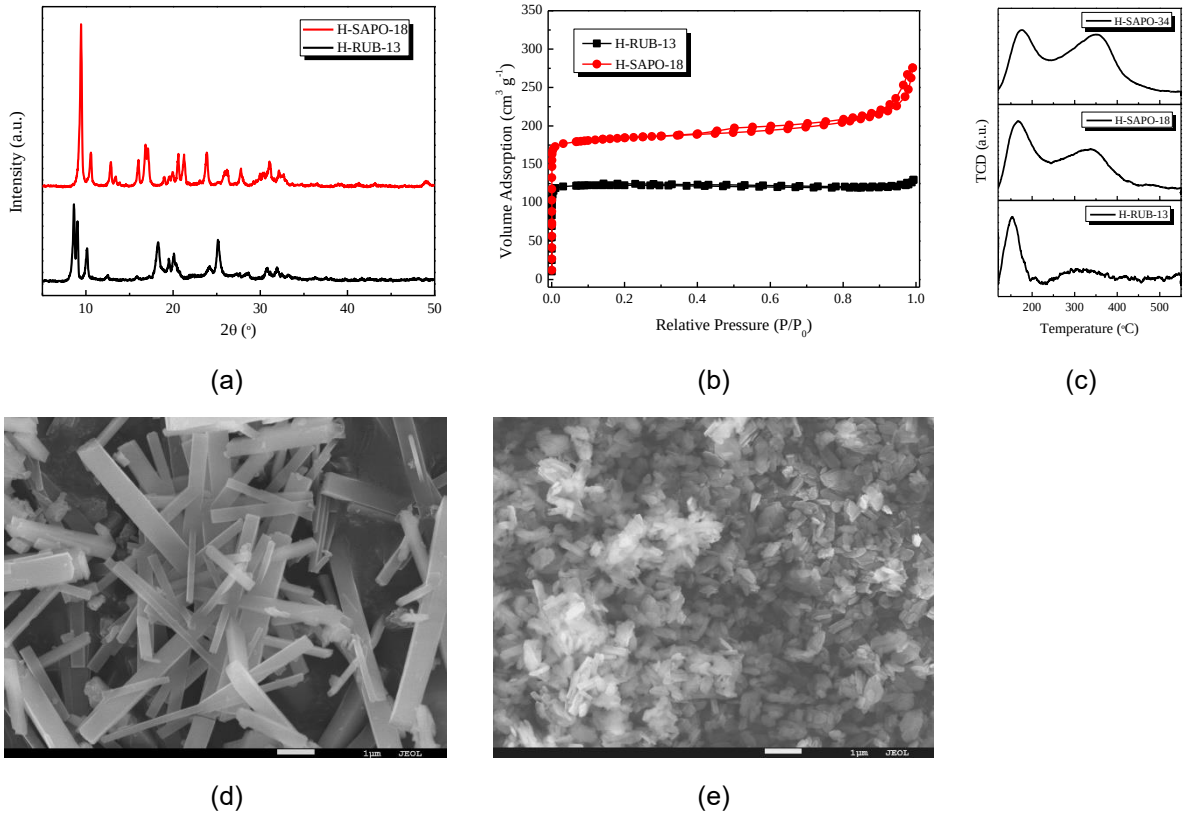

Figure S16. XRD patterns (a), N_2 sorption isotherms (b), NH_3-TPD profiles (c) and SEM images (d and e) of H-RUB-13 and H-SAPO-18 zeolites (d: H-RUB-13; e: H-SAPO-18).

Figure S17.

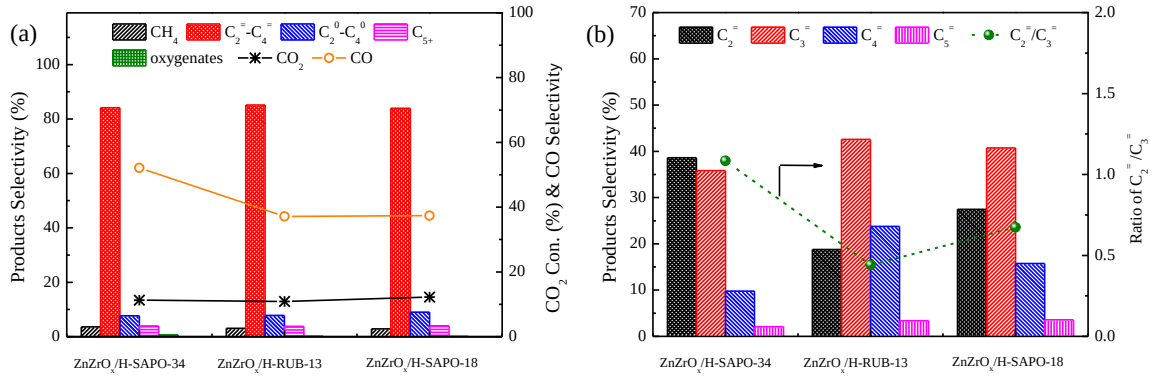

Figure S17. CO_2 conversion and product distribution obtained over $ZnZrO_x$/H-SAPO-34, $ZnZrO_x$/H-RUB-13 and $ZnZrO_x$/H-SAPO-18 composite catalysts (reaction conditions: H_2/CO_2 = 3:1, GHSV = 4000 mL/(g·h), 0.5 MPa, 370 °C).

Figure S18.

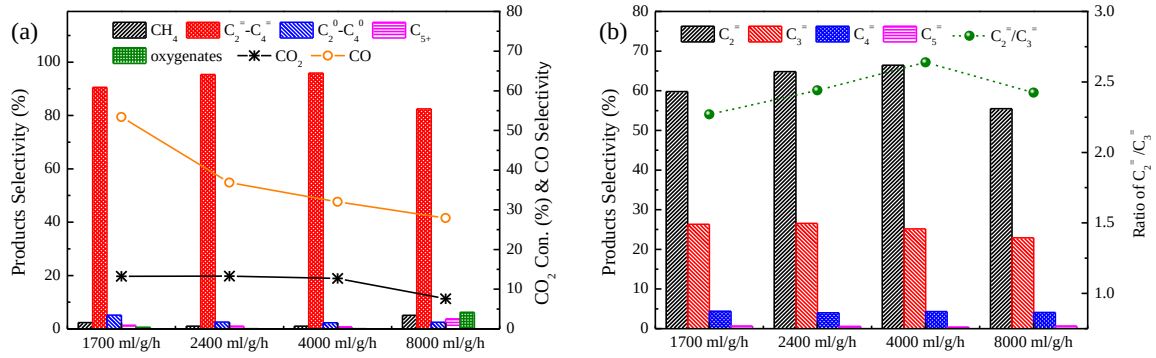

Figure S18. Effect of space velocity on the catalytic performance of Cr_2O_3(SG)/H-SAPO-34 composite catalyst for direct conversion of CO_2 into light olefins (reaction conditions: H_2/CO_2 = 3/1, 370 °C, 0.5 MPa).

Figure S19.

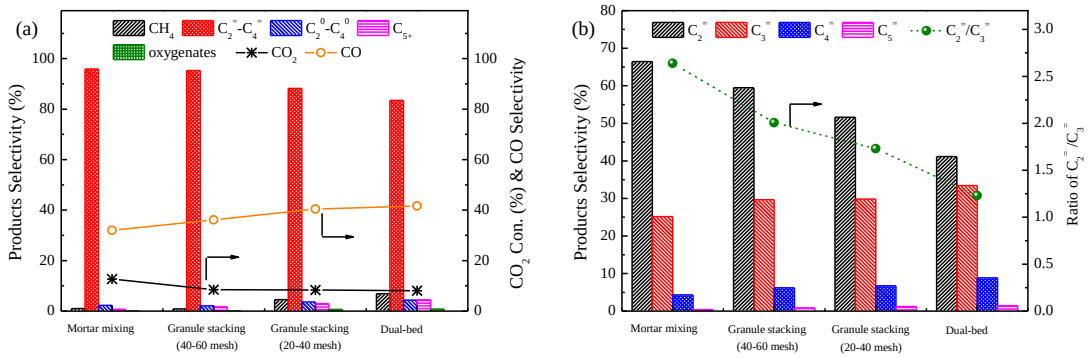

Figure S19. Effect of Cr_2O_3(SG) and H-SAPO-34 integration manner on the CO_2 conversion and the product distribution obtained in CO_2 hydrogenation to light olefins (typical reaction conditions: H_2/CO_2 = 3/1, GHSV = 4000 mL/(g·h), 0.5 MPa and 370 °C).

Figure S19 shows that increase of the contact distance between metal oxide and zeolite, more CO are produced. This results from the decline of the thermodynamic driving effect of acidic zeolite for formation of methanol and ethanol, but contrary enhancement of the competitive RWGS reaction or of CO formation.[5,10] The integration manner directly influences the distance between metal oxide and zeolite, and consequently, has an obvious effect on the catalytic performance, including CO selectivity.

Figure S20.

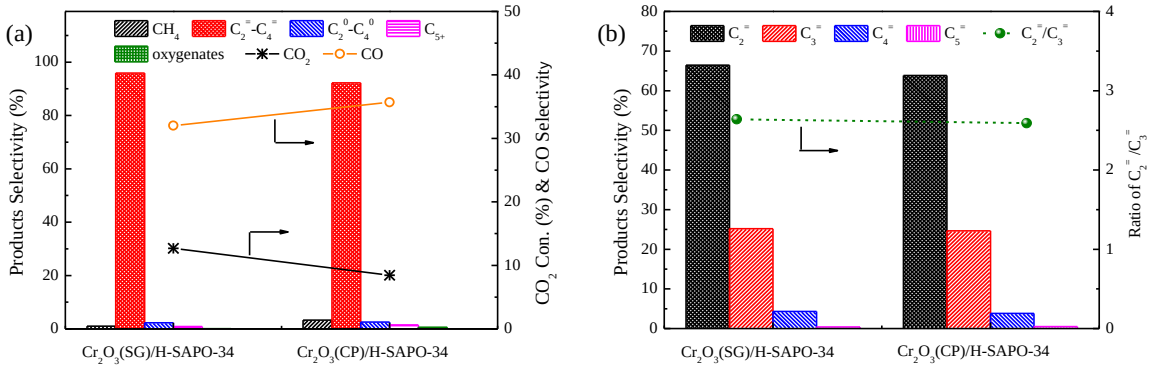

Figure S20. CO_2 conversions and product distributions obtained on the Cr_2O_3(SG)/H-SAPO-34 and Cr_2O_3(CP)/H-SAPO-34 composite catalysts respectively. Typical reaction conditions: H_2/CO_2 = 3:1, 370 °C, 0.5 MPa, GHSV = 4000 mL/(g·h).

The higher surface oxygen vacancy concentration of Cr_2O_3 (SG) than of Cr_2O_3(CP) makes Cr_2O_3(SG)/H-SAPO-34 show higher activity than Cr_2O_3(CP)/H-SAPO-34 in CO_2 hydrogenation to light olefins (Figures S20 and S21), but it does not have great effects on light olefins selectivity and distribution (ethene selectivity, 66.5% vs. 64.0%; propene selectivity, 25.0% vs. 24.7%; butene selectivity, 4.3% vs. 3.8%).

Figure S21.

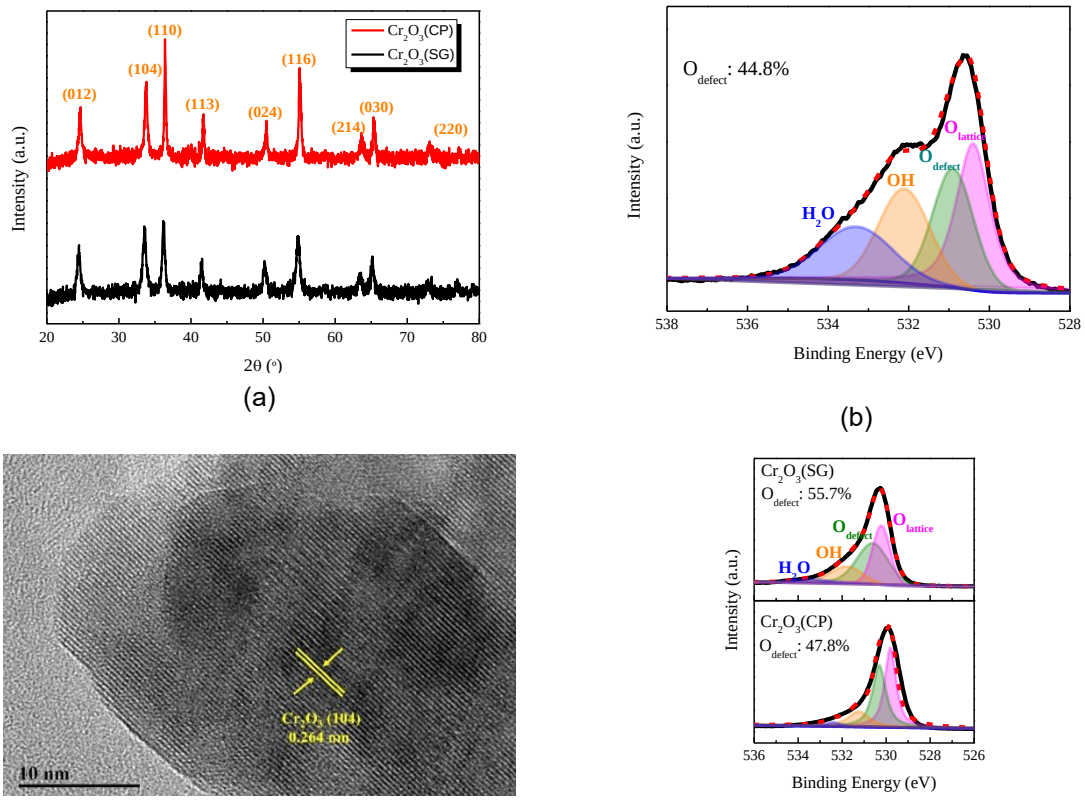

Figure S21. XRD patterns (a) of Cr_2O_3(SG) and Cr_2O_3(CP), and O(1s) XPS (b) and TEM image (c) of Cr_2O_3(CP), and in situ O(1s) XPS (d) of Cr_2O_3(SG) and Cr_2O_3(CP) oxides treated at 400 ºC for 2 h in H_2.

As is shown in Figures S1 and S21, and Table S1, Cr_2O_3(SG) has higher porosity and surface area, and larger concentration of surface oxygen vacancies than Cr_2O_3(CP), despite both the samples possess a similar crystal structure. After H_2 treatment, although the surface oxygen vacancy concentrations were increased for both the oxides (Figure S21d), Cr_2O_3(SG) (55.7%) still shows higher concentration of surface oxygen vacancies than Cr_2O_3(CP) (47.8%).

Figure S22.

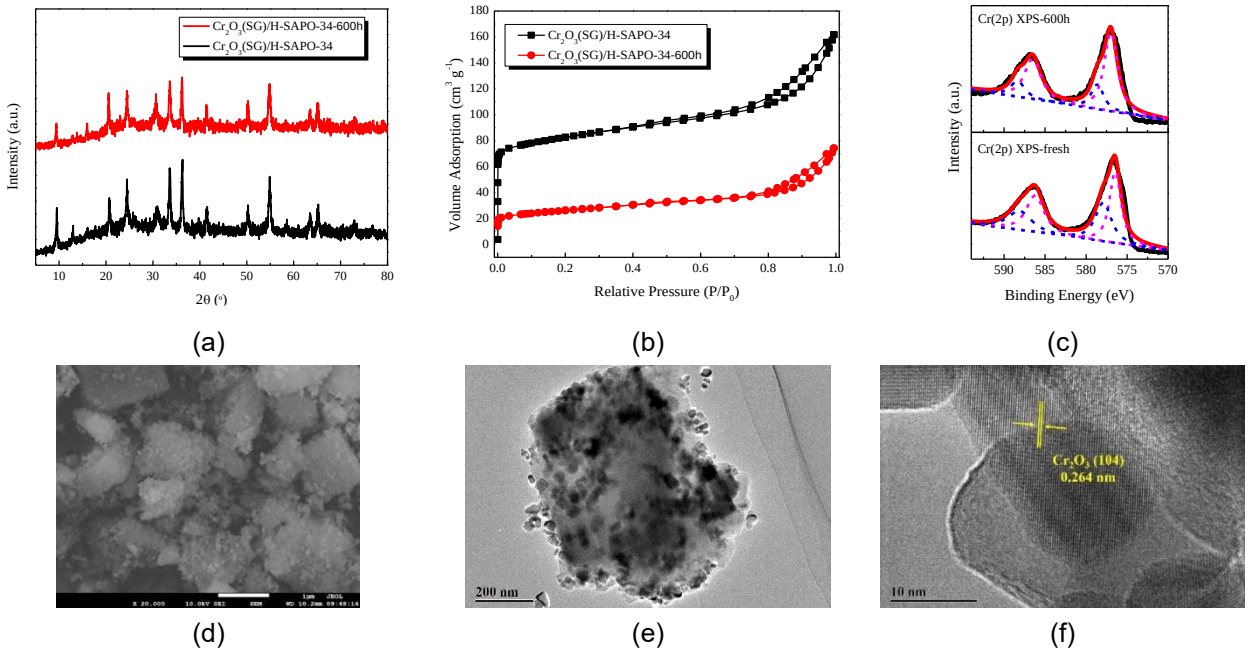

Figure S22. XRD patterns (a), N_2 sorption isotherms (b), Cr(2p) XPS (c) of fresh and used (catalyzing the reaction for 600 h) Cr_2O_3(SG)/H-SAPO-34, and SEM (d), TEM (e) and HRTEM images (f) of the used sample.

An interplanar spacing of 0.264 nm is clearly observed in the HRTEM image of Cr_2O_3(SG). It is correspondent to (104) crystal facet of Cr_2O_3. The Cr(2p) XPS indicates that most of the chromium species in Cr_2O_3(SG) are still Cr^{3+} even after 600 h (Figure S22).

Figure S23.

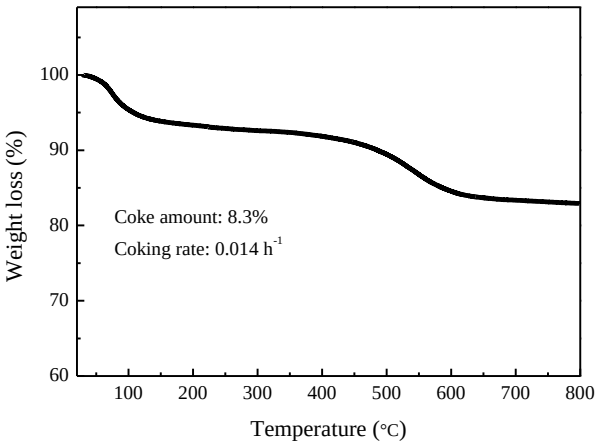

Figure S23. TG curve of Cr_2O_3(SG)/H-SAPO-34 composite after catalyzing the CO_2 hydrogenation to light olefins for 600 h (The data represent the weight loss at >250 ºC and coking rate (h^{-1})).

Figure S24.

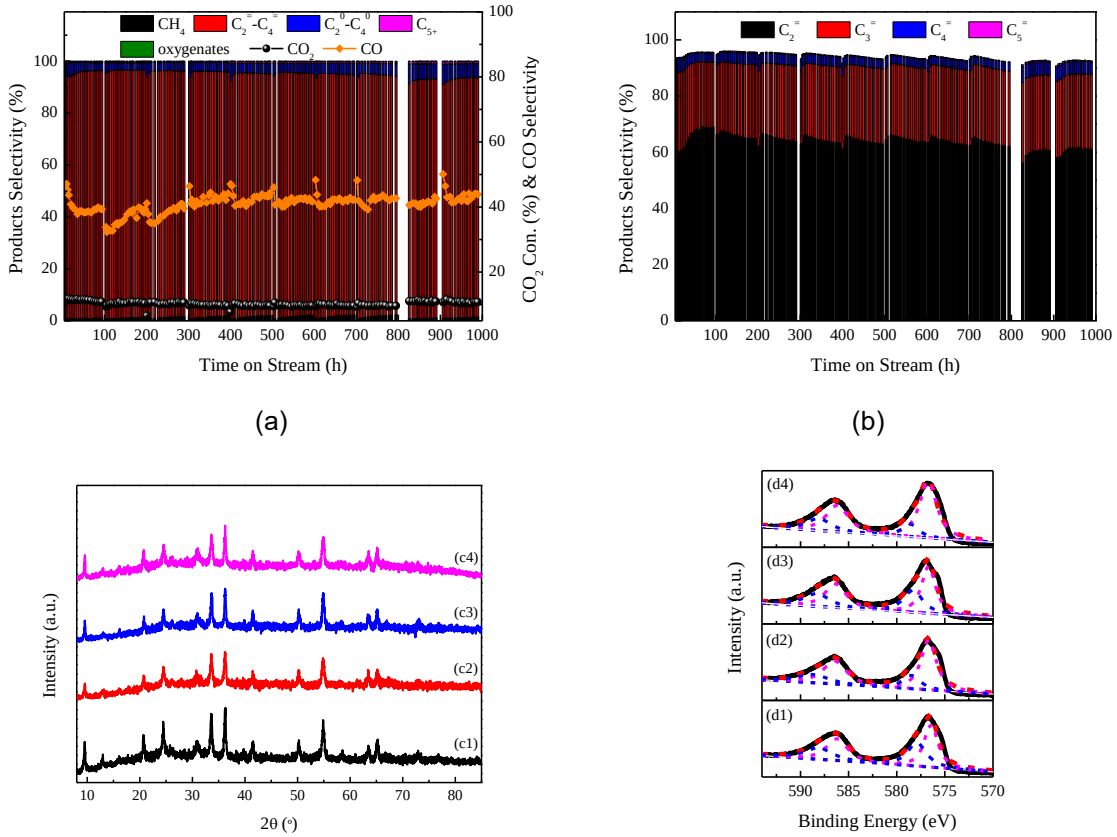

Figure S24. Catalytic repeatability. The catalytic results of Cr_2O_3(SG)/H-SAPO-34 (Si/Al = 0.15) for CO_2 hydrogenation to light olefins within 10 recycles with regeneration (a, b) (in the first eight recycles, the Cr_2O_3(SG)/H-SAPO-34 was regenerated at 550°C for 2 h in H_2 after catalyzing the reaction for 100 h in each run; in the last two recycles, it was firstly regenerated at 500°C for 0.5 h in 2%O_2/Ar mixture, and subsequently reduced at 550 °C for 2 h in H_2 after catalyzing the reaction for 100 h in each run) (reaction conditions: H_2/CO_2 = 3/1, 370 °C, 0.5 MPa and GHSV = 4000 mL/g·h); XRD patterns (c) and Cr(2p) XPS (d) of fresh (1), used for 8 recycles (2), and regenerated samples firstly at 500°C for 0.5 h in 2%O_2/Ar mixture (3) and subsequently reduced at 550 °C for 2 h in H_2 (4).

Figure S25.

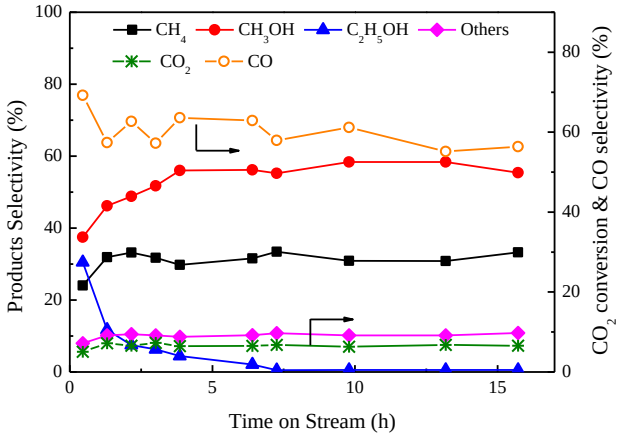

Figure S25. Catalytic results of Cr_2O_3(SG) for hydrogenation of CO_2. Typical reaction conditions: H_2/CO_2 = 3/1, 0.5 MPa, 370 °C and GHSV = 12000 mL/(g·h). The selectivity to CH_3OH is actually the selectivity to methanol and dimethyl ether. Others represent the sum of $C_2^{=}$ – $C_4^{=}$, C_2^0 – C_4^0 and C_5^+.

Table S7. Catalytic results of H-SAPO-34 for conversion of methanol, ethanol and their mixtures. [a]

Feedstocks [b]	Con. (%)	Product selectivity (%)								$C_2^=/C_3^=$
		CH_4	$C_2^=$-$C_4^=$	C_2^0-C_4^0	C_5+	$C_2^=$	$C_3^=$	$C_4^=$	$C_5^=$	
Methanol	85.0	1.6	90.0	0.7	7.7	25.6	45.7	18.7	3.1	0.56
Methanol/ethanol (12.75:1) [c]	80.0	1.0	95.9	0.6	2.5	45.9	35.5	14.5	1.2	1.29
Methanol/ethanol (2.44:1) [c]	84.0	0.7	95.0	0.7	3.6	60.0	25.3	9.7	1.9	2.37
Methanol/ethanol (1.60:1) [c]	76.5	0.6	96.2	0.9	2.3	71.8	17.4	7.0	1.7	4.12
Ethanol	85.0	0.1	99.2	0.4	0.3	98.4	0.6	0.2	0.1	164

[a] Reaction conditions: 370 ºC, WHSV = 28.5 h^{-1} and time on stream of around 1.0 – 3.0 h.

[b] The alcohol conversion was controlled below 90% for minimizing the effect of secondary reactions.[11,12]

[c] The methanol and ethanol mixture has methanol/ethanol mass ratios of 12.75:1, 2.44:1 and 1.60:1, respectively.

Figure S26.

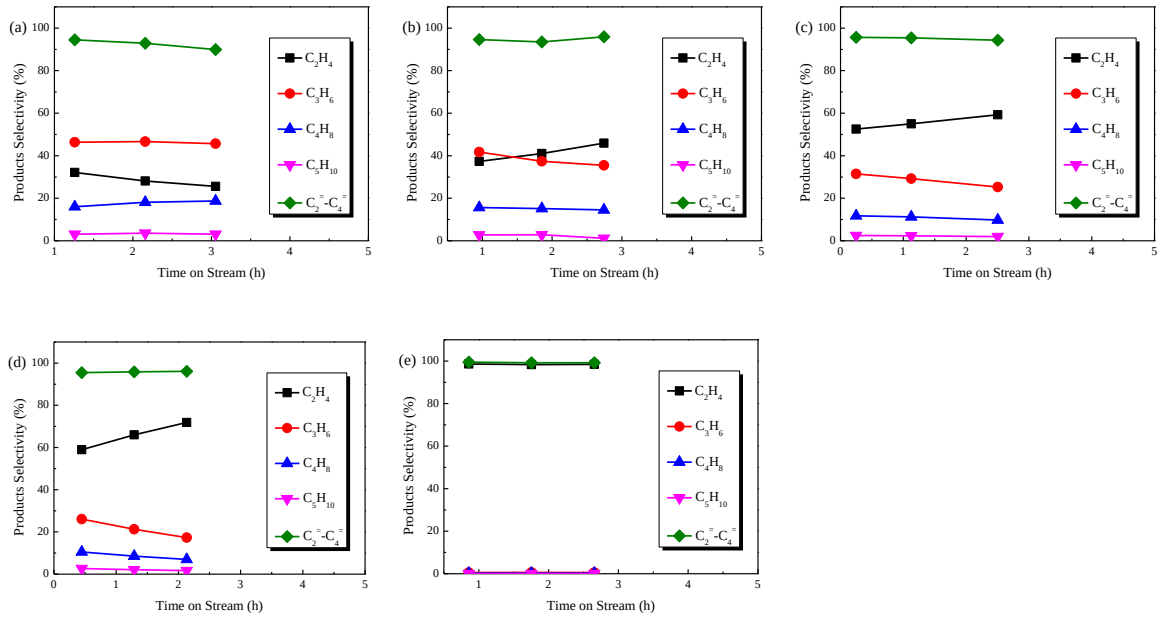

Figure S26. Product selectivity for conversion of methanol, ethanol and their mixture into light olefins over H-SAPO-34: methanol (a), methanol/ethanol mixture ((12.75/1) (b), 2.44:1 (c) and 1.60:1 (d)), and ethanol (e). Reaction conditions: 370 ºC, WHSV = 28.5 h^{-1}.

Figure S27.

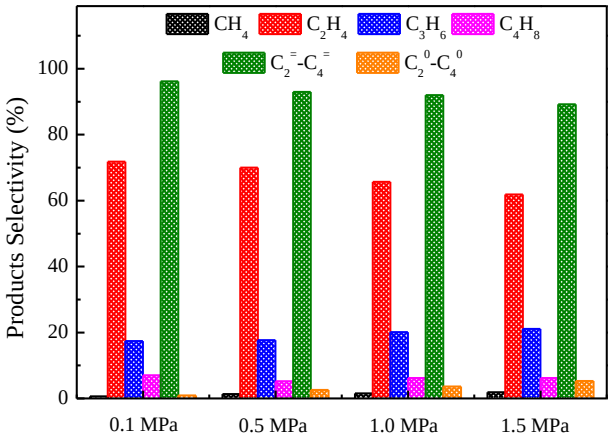

Figure S27. Product selectivity obtained over H-SAPO-34 in the conversion of methanol and ethanol mixture with a mass ratio of 1.6/1 into light olefins at different reaction pressure (reaction conditions: 370 ºC, WHSV = 28.5 h^{-1}).

Figure S28.

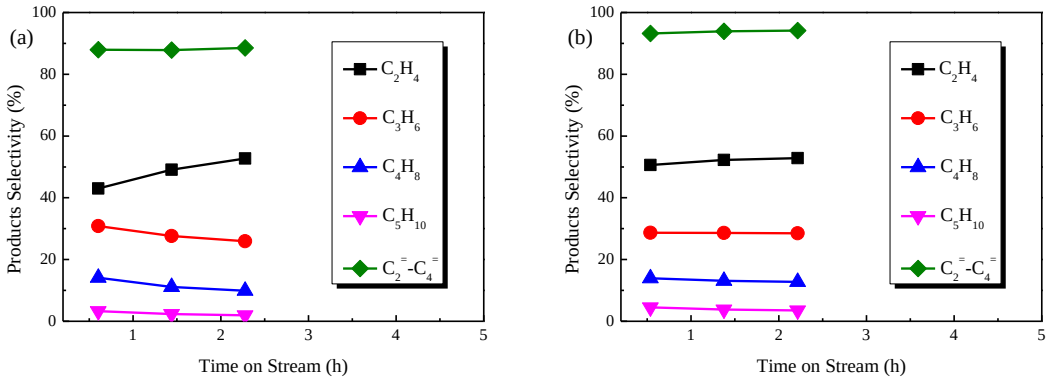

Figure S28. Product selectivity for conversion of methanol and ethanol mixture (methanol/ethanol mass ratio of 1.6/1) into light olefins on H-RUB-13 (a) and H-SAPO-18 (b) (reaction conditions: 370 ºC and WHSV = 28.5 h^{-1}).

Figure S29.

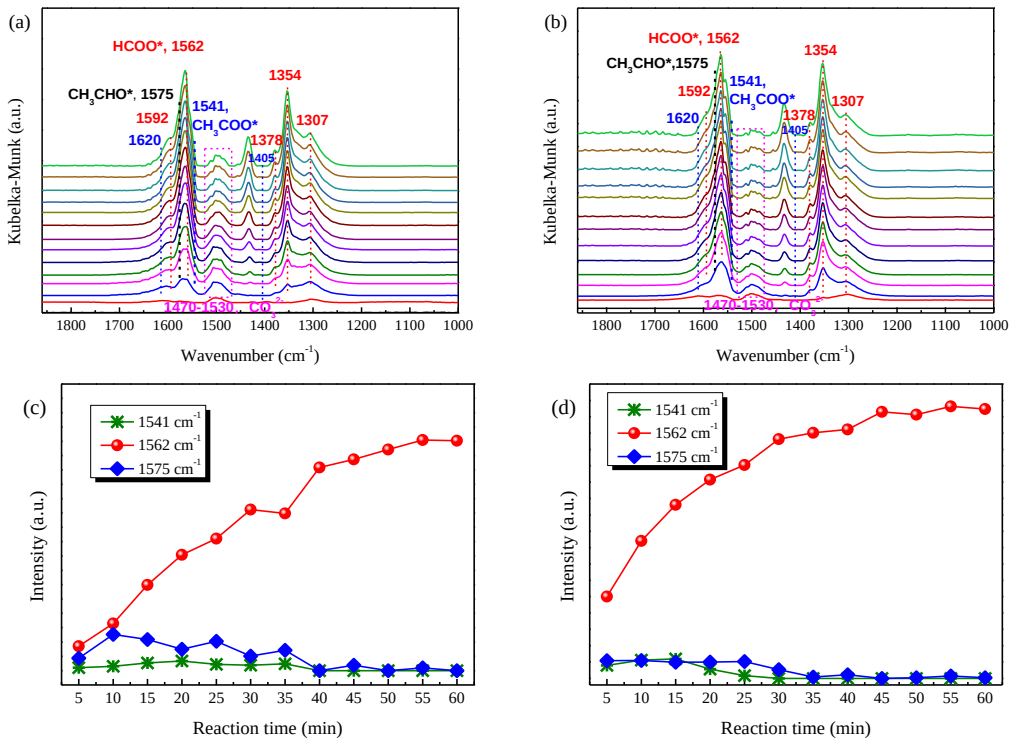

Figure S29. Time-dependent DRIFT spectra for hydrogenation of CO_2 on Cr_2O_3(SG). The spectra was collected every 5 min up to 60 min after pre-treating the sample with H_2 (30 mL/min) for 2 h at 400 °C and purging with Ar (30 mL/min) for 0.5 h at 340 °C (a) and 370 °C (b) (typical reaction conditions: 340 or 370 °C, 0.1 MPa); intensity evolutions of the peaks characteristic of formate, acetate and acetaldehyde with the reaction time on Cr_2O_3(SG) at 340 °C (c) and 370 °C (d) in CO_2 hydrogenation.

Figure S30.

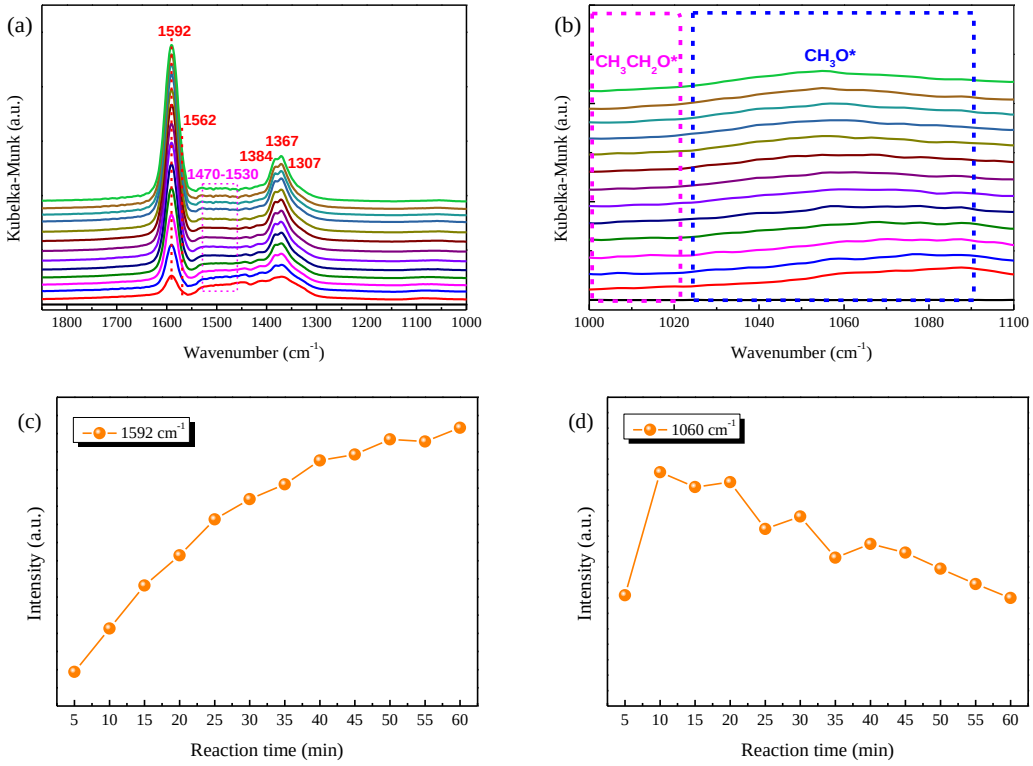

Figure S30. Time-dependent DRIFT spectra for hydrogenation of CO_2 on $ZnZrO_x$ oxide ((a) and (b)). The spectra was collected every 5 min up to 60 min after pre-treating the sample with H_2 (30 mL/min) for 2 h at 400 °C and purging with Ar (30 mL/min) for 0.5 h at 300 °C (typical reaction conditions: 300 °C, 0.1 MPa); intensity evolutions of the peaks characteristic of formate (c) and methoxy (d) with the reaction time on $ZnZrO_x$ oxide at 300 °C in CO_2 hydrogenation.

Table S8. Calculated free energy barriers ($\Delta G_{int}^{\neq}$), enthalpy barriers ($\Delta H_{int}^{\neq}$) and entropy losses ($-T\Delta S_{int}^{\neq}$) for formation of methanol (CH_3OH) and ethanol (C_2H_5OH) on pure Cr_2O_3 at 300 ºC.

Steps	$\Delta G_{int}^{\neq}$ (eV)	$\Delta H_{int}^{\neq}$ (eV)	$-T\Delta S_{int}^{\neq}$ (eV)
Methanol synthesis			
TS1	0.84	0.67	0.17
TS2	1.32	1.16	0.16
TS3	1.24	1.18	0.06
TS4	0.70	0.64	0.06
TS5	0.62	0.39	0.23
TS6	1.45	1.44	0.01
Ethanol synthesis			
TS1*	1.74	1.83	–0.09
TS2*	1.25	1.14	0.11
TS3*	1.31	1.44	–0.13
TS4*	1.35	1.19	0.16
TS5*	1.44	1.52	–0.08

Figure S31.

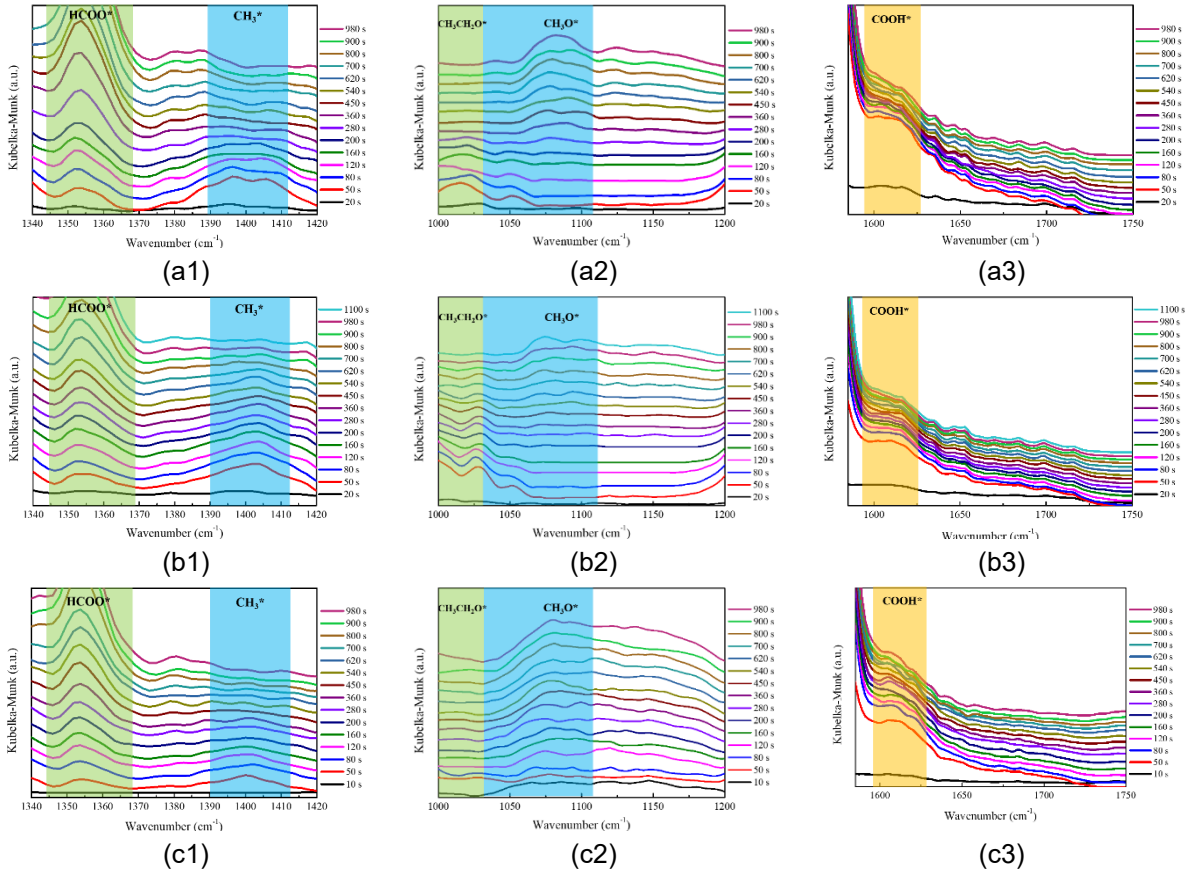

Figure S31. Time-dependent DRIFT spectra for hydrogenation of CO_2 on Cr_2O_3(SG) at 300 °C (a), 280 °C (b) and 320 °C (c), as collected at a resolution of 4 cm^{-1} by accumulating 32 scans. The collection time for each spectrum is less than 20 s.

Figure S32.

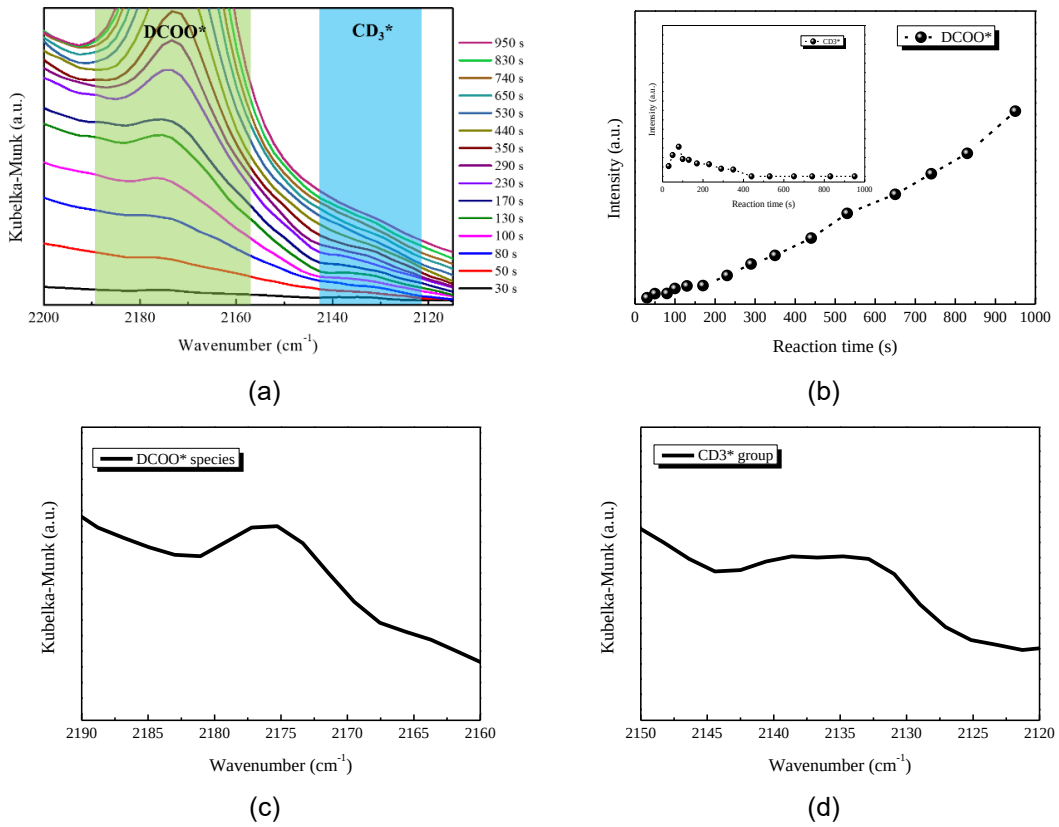

Figure S32. Isotope-labeled in situ DRIFTS. Time-dependent DRIFT spectra of Cr_2O_3(SG) for CO_2 + D_2 reaction at 300 °C, as collected at a resolution of 4 cm^{-1} by accumulating 32 scans (a); intensity evolutions of the bands assigned to DCOO* (between 2160 and 2190 cm^{-1}) and CD_3* group (insert, between 2120 and 2150 cm^{-1}) species with the reaction time (b); magnified DRIFT spectra in the ranges of 2160−2190 cm^{-1} and of 2120−2150 cm^{-1} collected at reaction time of 30 s ((c) and (d)).

Figure S33.

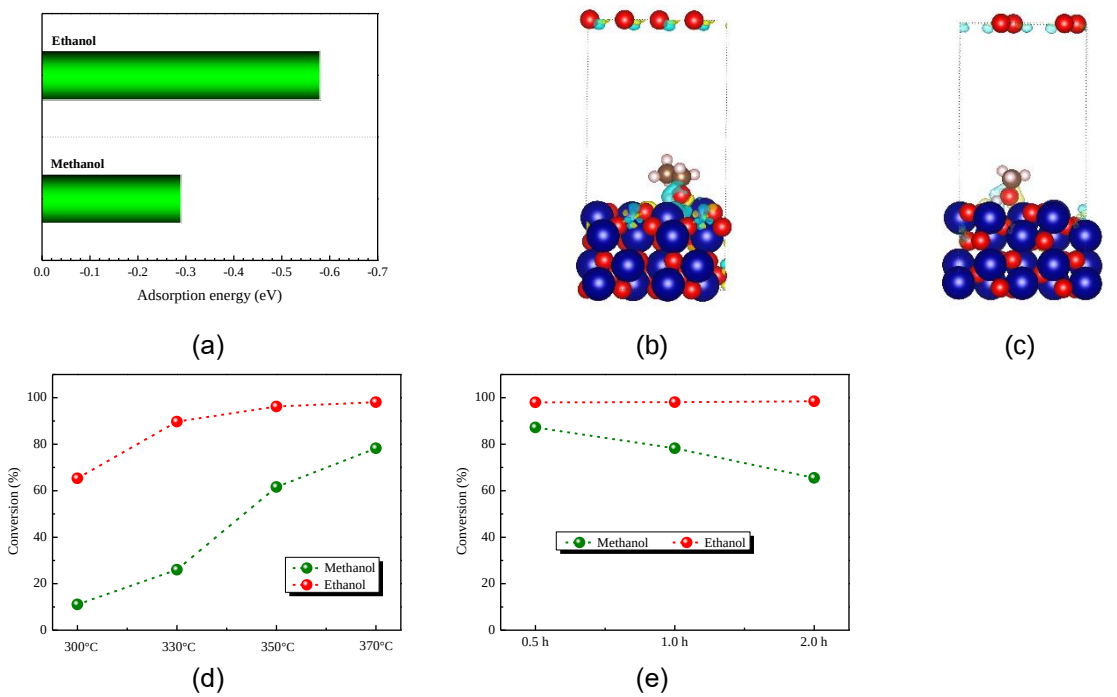

Figure S33. Calculated adsorption energy (a) and charge difference density (CDD) of ethanol (b) and methanol (c) on Cr_2O_3 (the accumulation and depletion charge regions are shown in yellow and cyan respectively in CDD); the conversions of ethanol and methanol at different reaction temperatures (d) and time (e) over H-SAPO-34.

Figure S34.

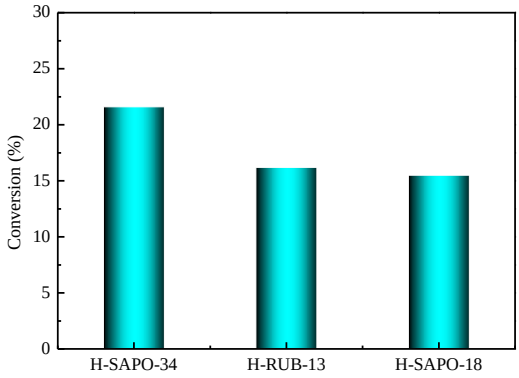

Figure S34. Conversions of methanol and ethanol for transformation of methanol and ethanol mixture (methanol/ethanol mass ratio of 1.6/1) on H-SAPO-34, H-RUB-13 and H-SAPO-18 at 300 °C, 0.5 h and WHSV of 6 h^{-1}.

Figure S35.

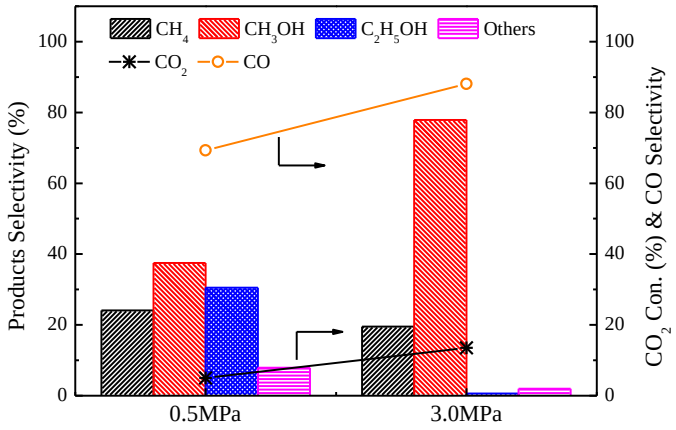

Figure S35. Catalytic results of Cr_2O_3(SG) for hydrogenation of CO_2 at 0.5 and 3.0 MPa. Typical reaction conditions: H_2/CO_2 = 3/1, 370 °C, GHSV = 12000 mL/(g·h) and time on stream of 0.5 h. The selectivity for CH_3OH is actually the selectivity to methanol and dimethyl ether. Others represent the sum of $C_2^{=}$ – $C_4^{=}$, C_2^{0} – C_4^{0} and C_5^{+}.

Table S9. Calculated free energy barriers ($\Delta G_{int}^{\neq}$), enthalpy barriers ($\Delta H_{int}^{\neq}$) and entropy losses ($-T\Delta S_{int}^{\neq}$) for methane (CH_4) formation on pure Cr_2O_3 at 300 ºC via CO dissociation and subsequent hydrogenation.

Steps	$\Delta G_{int}^{\neq}$ (eV)	$\Delta H_{int}^{\neq}$ (eV)	$-T\Delta S_{int}^{\neq}$ (eV)
CO+H*→COH* (TS1)	1.10	1.19	–0.09
COH*→C*+OH* (TS2)	1.56	1.58	–0.02
C*+H*→CH* (TS3)	1.63	1.37	0.26
CH*+H*→CH_2* (TS4)	1.71	1.44	0.27
CH_2*+H*→CH_3* (TS5)	1.36	1.24	0.12
CH_3*+H*→CH_4* (TS6)	1.40	1.42	–0.02

Figure S36.

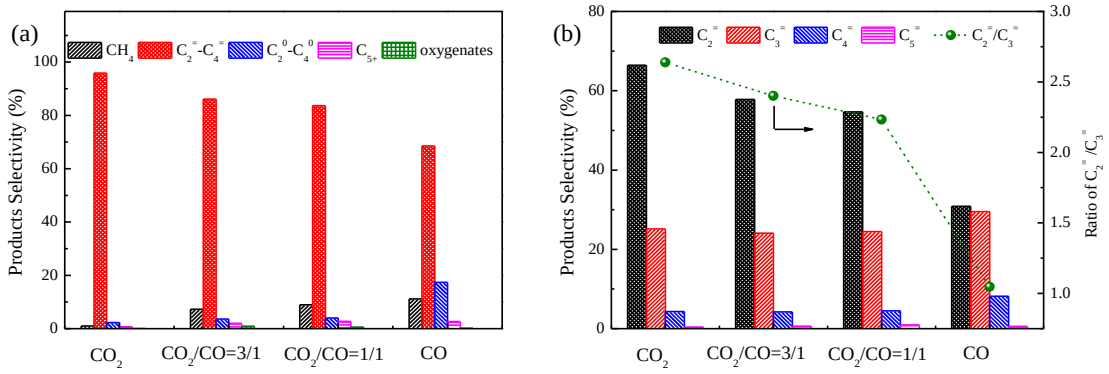

Figure S36. Catalytic results of Cr_2O_3(SG)/H-SAPO-34 composite for conversion of CO_2, CO_2+CO mixture (volume ratio of CO_2 to CO is 3/1 and 1/1) or CO into light olefins. Typical reaction conditions: H_2/(CO_2 and/or CO) = 3/1, 370 °C, 0.5 MPa and GHSV = 4000 mL/(g·h)).

Figure S37.

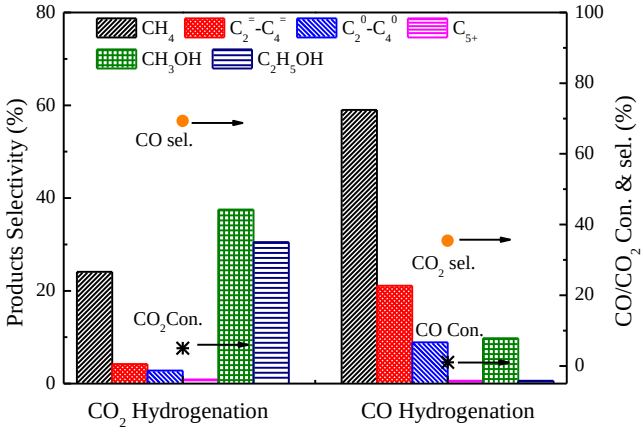

Figure S37. Catalytic results of Cr_2O_3(SG) for hydrogenations of CO_2 and CO. Typical reaction conditions: H_2/(CO_2 or CO) = 3/1, 370 °C, 0.5 MPa, GHSV = 12000 mL/(g·h) and time on stream of 0.5 h. The selectivity for CH_3OH is actually the selectivity to methanol and dimethyl ether.

Figure S38.

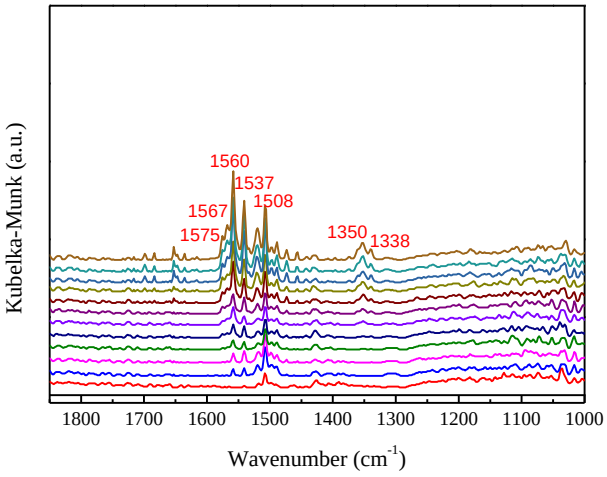

Figure S38. Time-dependent DRIFT spectra for hydrogenation of CO on Cr_2O_3(SG). The spectra was collected every 5 min up to 60 min after pre-treating the sample with H_2 (30 mL/min) for 2 h at 400 °C and purging with Ar (30 mL/min) for 0.5 h at 300 °C. Typical reaction conditions: 300 °C and 0.1 MPa.

Table S10. Calculated adsorption energies of CO_2 and CO on Cr_2O_3 oxide.

	CO_2	CO
Adsorption energy (eV)	–0.278	–0.125

Figure S39.

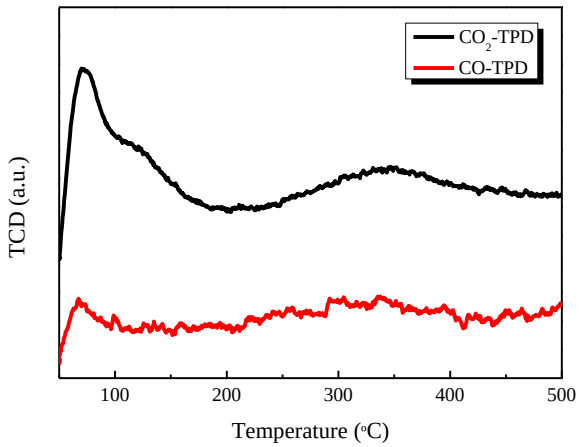

Figure S39. CO_2-TPD and CO-TPD profiles of Cr_2O_3(SG).

Figure S40.

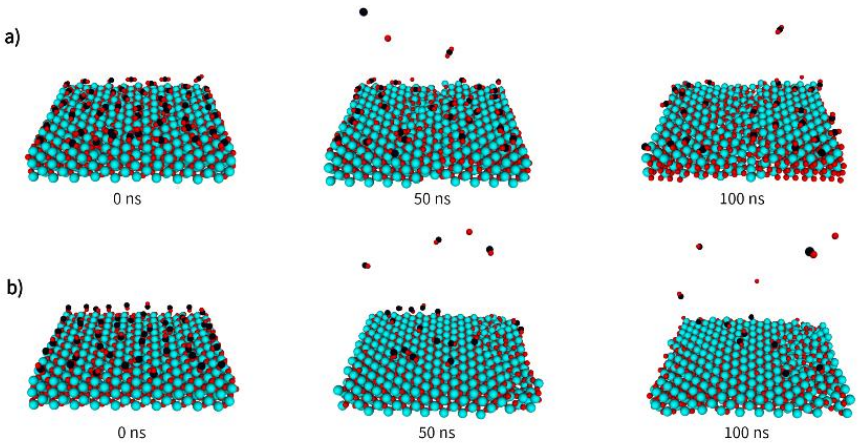

Figure S40. Optimized structure scheme for co-adsorption of CO_2 and CO on Cr_2O_3 oxide, as obtained by molecular dynamic (MD) simulation at 370 °C and 0.5 MPa (Atoms coloring: red (O), green (Cr) and black (C)). (a) CO_2/CO molar ratio of 45/5 and (b) CO_2/CO molar ratio of 1/49.

Supplemental Experimental Procedures

Catalyst characterization. The crystal structure of samples was examined by X-ray diffraction (XRD) technique (Bruker D8 Advance X-ray diffractometer, CuKα radiation (λ = 1.5418 Å), 40 kV and 40 mA). The patterns were recorded at a scanning rate of 2°·min^{-1} in the 2θ range of 5° − 85°. In situ XRD patterns were measured by loading the sample in a self-made cell. Before the measurement, the sample was pretreated at 400 ºC for 2 h in a H_2 flow (30 mL/min), and then purged with an Ar (30 mL/min) flow for 0.5 h. After the sample was cooled to reaction temperature (370 ºC), the CO_2 and H_2 mixture (CO_2/H_2 = 1/3) was fed into the in situ cell. The XRD patterns were collected every 5 h up to 25 h. The Rietveld refinement was performed by using the HighScore plus software and the average particle size was calculated by the Scherrer equation.

Field emission-scanning electron microscopy (FE-SEM) images were taken on a JEOL JSM-7900F instrument. High-resolution transmission electron microscopy (HRTEM) and TEM images were measured on a field emission-transmission electron microscope (JEM-2100F, JEOL). The average particle size was estimated by counting more than 100 particles in the TEM images. The scanning transmission electron microscopy images were acquired at 200 kV on a JEOL JEM-2100F instrument using a high-angle annular dark field detector (STEM-HAADF), and the elemental distribution of the samples was analyzed by the energy-dispersive X-ray spectroscopy (EDX) detector.

The surface areas, pore volumes and pore size distributions of samples were measured by N_2 sorption that was carried out at −196 °C on a Micrometritics TriStar II 3020 instrument. Prior to the measurement, the samples were degased at 250 °C for 8 h. The total surface area was calculated from adsorption branch in the relative pressure range of 0.05 – 0.25 by the Brunauer−Emmett−Teller (BET) method, the pore volume was calculated from desorption branch by the t-Plot method, and the pore size distribution was estimated by the BJH method. The O(1s) and Cr(2p) X-ray photoelectron spectra (XPS) were measured under ultrahigh vacuum (5 × 10^{-7} Pa) on an AXIS ULTRA DLD instrument equipped with an AlKα monochromator X-ray source (hv = 1486.6 eV), and calibrated with the binding energy of carbon deposit C(1s) (E_b = 284.6 eV). The concentration of surface oxygen vacancies is defined as, $O_{defect} = I_{Odefect}/(I_{Odefect} + I_{Olattice})$, where $I_{Odefect}$ and $I_{Olattice}$ correspond to the intensity of peaks at around 531.0 and 530.3 eV in O(1s) XPS, which are assigned to O vacancies (O_{defect}) and lattice oxygen species ($O_{lattice}$), respectively.[13]

Temperature-programmed reduction by hydrogen (H_2-TPR) was conducted on a Micromeritics AutoChem II 2920. 0.1 g Sample was loaded into a U-shaped quartz reactor and pretreated at 300 °C for 1 h in a He flow (30 mL/min) to remove surface impurities. After being cooled down to room temperature, the sample was exposed to a 10% H_2/Ar flow (30 mL/min) and heated to 800 °C at a rate of 10 °C/min. The effluent was analyzed by a thermal conductivity detector (TCD).

The temperature-programmed desorption of CO_2 (CO_2-TPD) was also carried out on the Micrometritics AutoChem II 2920 apparatus. 0.1 g Sample was loaded into a U-type tube and pretreated at 300 °C for 1 h in a He flow. Then, the sample was cooled to room temperature and allowed to fully adsorb CO_2 that was pulse injected. After the sample was swept with He, the temperature was ramped from 50 to 600 °C at a rate of 10 °C/min, and the desorbed CO_2 was monitored by a TCD.

The time-dependent diffuse reflectance infrared Fourier transform (DRIFT) spectra was recorded on a Bruker vertex 80 spectrometer equipped with a liquid nitrogen-cooled MCT detector and a high-temperature reaction cell. First, 50 mg sample was placed in the cell and pretreated at 400 ºC for 2 h in a H_2 flow (30 mL/min). Then, it was purged with Ar (30 mL/min) for 0.5 h. Afterwards, it was cooled to the reaction temperature of 300, 340 or 370 ºC and the background spectrum was collected. Finally, it was exposed to a CO_2 and H_2 gaseous mixture flow (CO_2/H_2 = 1/3, flow rate = 40 mL/min) at the reaction temperature, and the spectra were collected every 5 min up to 60 min at a resolution of 4 cm^{-1} by accumulating 64 scans. At real reaction temperature, e.g. 370 ºC, some intermediate species, such as CH_3*, CH_3CHO* and CH_3COO*, are highly unstable, and hence, are very difficult to be detected. Thus, in situ DRIFTS measurements were carried out at relative low temperature of 280−370 ºC for facilely observing the formation and evolution of reaction intermediates.[5,14−16]

The CO_2 hydrogenation was carried out according to the following procedures. 0.2 g Sample was placed in a stainless-steel tubular reactor and pretreated at 400 °C for 2 h in a H_2 flow (30 mL/min). Then, it was cooled to the reaction temperature (370 °C) and flushed with an Ar flow (30 mL/min) for 0.5 h. This is followed by exposing to a CO_2 and H_2 gaseous mixture flow (CO_2/H_2 = 1/3, flow rate = 40 mL/min) at the reaction temperature. The effluent was on-line collected in a gas bag and analyzed by a Shimadzu Ultra QP2010 GC-MS spectrometer equipped with a HP-PLOT-Q capillary column.

Supplemental References

(1) Gao, P., Dang, S. S., Li, S. G., Bu, X. N., Liu, Z. Y., Qiu, M. H., Yang, C. G., Wang, H., Zhong, L. S., Han, Y., Liu, Q., Wei, W. and Sun, Y. H. (2018). Direct production of lower olefins from CO_2 conversion via bifunctional catalysis. ACS Catal. *8*, 571−578.

(2) Dang, S. S., Gao, P., Liu, Z. Y., Chen, X. Q., Yang, C. G., Wang, H., Zhong, L. S., Li, S. G. and Sun, Y. H. (2018). Role of zirconium in direct CO_2 hydrogenation to lower olefins on oxide/zeolite bifunctional catalysts. J. Catal. *364*, 382–393.

(3) Gao, J. J., Jia, C. M. and Liu, B. (2017). Direct and selective hydrogenation of CO_2 to ethylene and propene by bifunctional catalysts. Catal. Sci. Technol. *7*, 5602–5607.

(4) Numpilai, T., Wattanakit, C., Chareonpanich M. and Limtrakul, J. (2019). Optimization of synthesis condition for CO_2 hydrogenation to light olefins over In_2O_3 admixed with SAPO-34. Energ. Convers. Manage. *180*, 511–523.

(5) Li, Z. L., Wang, J. J., Qu, Y. Z., Liu, H. L., Tang, C. Z., Miao, S., Feng, Z. C., An, H. Y. and Li, C. (2017). Highly selective conversion of carbon dioxide to lower olefins. ACS Catal. *7*, 8544−8548.

(6) Liu, X. L., Wang, M. H., Zhou, C., Zhou, W., Cheng, K., Kang, J. C., Zhang, Q. H., Deng, W. P. and Wang, Y. (2018). Selective transformation of carbon dioxide into lower olefins with a bifunctional catalyst composed of $ZnGa_2O_4$ and SAPO-34. Chem. Commun. *54*, 140−143.

(7) Liu, X. L., Wang, M. H., Yin, H. R., Hu, J. T., Cheng, K., Kang, J. C., Zhang, Q. H. and Wang, Y. (2020). Tandem catalysis for hydrogenation of CO and CO_2 to lower olefins with bifunctional catalysts composed of spinel oxide and SAPO-34. ACS Catal. *10*, 8303−8314.

(8) Wang, J. Y., Zhang, A. F., Jiang, X., Song, C. S. and Guo, X. W. (2018). Highly selective conversion of CO_2 to lower hydrocarbons (C_2-C_4) over bifunctional catalysts composed of In_2O_3-ZrO_2 and zeolite. J. CO_2 Util. *27*, 81–88.

(9) Chen, J. Y., Wang, X., Wu, D. K., Zhang, J. L., Ma, Q. X., Gao, X. H., Lai, X. Y., Xia, H. Q., Fan, S. B. and Zhao, T. S. (2019). Hydrogenation of CO_2 to light olefins on CuZnZr@(Zn-)SAPO-34 catalysts: Strategy for product distribution. Fuel. *239*, 44–52.

(10) Jiang, H. J., Hou, Z. H. and Luo, Y. (2020). A kinetic view on proximity-dependent selectivity of carbon dioxide reduction on bifunctional catalysts. ACS Catal. *10*, 13518−13523.

(11) Bleken, F. L., Janssens, T. V. W., Svelle, S. and Olsbye, U. (2012). Product yield in methanol conversion over ZSM-5 is predominantly independent of coke content. Micropor. Mesopor. Mater. *164*, 190–198.

(12) Shen, Y. F., Le, T. T., Fu, D. L., Schmidt, J. E., Filez, M., Weckhuysen, B. M. and Rimer, J. D. (2018). Deconvoluting the competing effects of zeolite framework topology and diffusion path length on methanol to hydrocarbons reaction. ACS Catal. *8*, 11042–11053.

(13) Liang, F., Yu, Y., Zhou, W., Xu, X. and Zhu, Z. (2015). Highly defective CeO_2 as a promoter for efficient and stable water oxidation. J. Mater. Chem. A *3*, 634−640.

(14) Liu, X. L., Zhou, W., Yang, Y. D., Cheng, K., Kang, J. C., Zhang, L., Zhang, G. G., Min, X. J., Zhang, Q. H. and Wang, Y. (2018). Design of efficient bifunctional catalysts for direct conversion of syngas into lower olefins via methanol/dimethyl ether intermediates. Chem. Sci. *9*, 4708–4718.

(15) Wu, X. Q., Xu, S. T., Zhang, W. N., Huang, J. D., Li, J. Z., Yu, B. W., Wei, Y. X. and Liu, Z. M. (2017). Direct mechanism of the first carbon–carbon bond formation in the methanol-to-hydrocarbons process. Angew. Chem. Int. Ed. *56*, 9039–9043.

(16) Yang, L., Yan, T. T., Wang, C. M., Dai, W. L., Wu, G. J., Hunger, M., Fan, W. B., Xie, Z. K., Guan, N. J. and Li, L. D. (2019). Role of acetaldehyde in the roadmap from initial carbon−carbon bonds to hydrocarbons during methanol conversion. ACS Catal. *9*, 6491−6501.